HHS Public Access

Author manuscript

Proc SPIE Int Soc Opt Eng. Author manuscript; available in PMC 2019 September 27.

Published in final edited form as:

Proc SPIE Int Soc Opt Eng. 2017 February ; 10132: . doi:10.1117/12.2253935.

A Patch-based CBCT Scatter Artifact Correction Using Prior CT

Xiaofeng Yang[1,*], **Tian Liu**[1], **Xue Dong**[1], **Xiangyang Tang**[2], **Eric Elder**[1], **Walter J. Curran**[1], **Anees Dhabaan**[1]

[1]Department of Radiation Oncology and Winship Cancer Institute, Emory University, Atlanta, GA

[2]Department of Radiology and Imaging Sciences and Winship Cancer Institute, Emory University, Atlanta, GA

Abstract

We have developed a novel patch-based cone beam CT (CBCT) artifact correction method based on prior CT images. First, we used the image registration to align the planning CT with the CBCT to reduce the geometry difference between the two images. Then, we brought the planning CT-based prior information into the Bayesian deconvolution framework to perform the CBCT scatter artifact correction based on patch-wise nonlocal mean strategy. We evaluated the proposed correction method using a Catphan phantom with multiple inserts based on contrast-to-noise ratios (CNR) and signal-to-noise ratios (SNR), and the image spatial non-uniformity (ISN). All values of CNR SNR and ISN in the corrected CBCT image were much closer to those in the planning CT images. The results demonstrated that the proposed CT-guided correction method could significantly reduce scatter artifacts and improve the image quality. This method has great potential to correct CBCT images allowing its use in adaptive radiotherapy.

Keywords

CT; CBCT; scatter artifact correction; deconvolution

1. INTRODUCTION

Quantitative cone-beam CT (CBCT) imaging is on increasing demand for precise image guided radiation therapy since it provides a foundation for advanced image-guidance techniques, including accurate treatment setup, online tumor delineation and patient dose calculation [1, 2]. With more precise treatment monitoring from accurate CBCT images, dose delivery errors can be significantly reduced in each fraction and further compensated for in subsequent fractions using adaptive radiation therapy. However, the current CBCT imaging has severe artifacts mainly due to scatter contamination and its current clinical application is therefore limited to patient setup based on only bony structures [3, 4]. Artifacts assumed to be associated with scatter, such as cupping and streaking, can easily be observed from reconstructed patient images in clinical studies [4, 5]. Various scatter correction methods have been developed and can be categorized into two general types: scatter suppression and scatter estimation [6, 7]. Scatter suppression techniques, such as

*Corresponding authors: xyang43@emory.edu.

using anti-scatter grids and increasing the air gap, attempt to reduce the number of scatter photons that reach the detector array [8, 9]. Scatter estimation techniques attempt to remove the scatter photons from the acquired projection images using analytical or empirical predictions of scatter distribution, such as deconvolution [6, 10], offline calibration [7], Monte Carlo [11] and hybrid techniques [12, 13].

X-ray scatter can be approximated as a convolution of the primary signal by a blurring kernel [14], and thereafter it can be estimated and removed by deconvolution methods. Deconvolution methods are relatively easy to implement; usually, no additional hardware or acquisition time is required and no additional dose is given to the patient [15]. We proposed a scatter artifact correction method using a patch-based Bayesian deconvolution framework to improve the CBCT image quality. In the current radiotherapy workflow, a planning CT is usually required to acquire before radiotherapy to generate treatment plans. We utilized the acquired planning CT to provide the prior knowledge of true objects for Bayesian framework to iteratively perform scatter artifact correction for CBCT mages. This proposed approach has 2 distinctive strengths: 1) Instead of suffering from the accuracy of anatomical image segmentation, the proposed method introduced a patch-based nonlocal mean strategy to capture the prior information from planning CT to guide the scatter correction of CBCT images; 2) Contrary to classical Bayesian framework, the proposed method is derived in a Bayesian framework with an Markov Random Field (MRF) model for prior information regularization.

2. METHODS

In the proposed method, image registration is firstly used to reduce the geometry difference between the two images. The planning CT-based prior information using patch-based nonlocal mean strategy is added into Bayesian deconvolution framework to iteratively perform scatter artifact correction for CBCT mages. The three major steps are briefly described below.

2.1 Bayesian-based Deconvolution Framework

Assume $i(r)$ is the CBCT image after scanning a true spatial distribution of point object o(r) by a CBCT scanner with a 3D point spread function of$h(r)$ [16]. r is the 3D coordinate of an image voxel. Under these conditions, CBCT imaging is a convolution process and is modeled as

$$i(r) = o(r) \otimes h(r) + n(r) \quad (1)$$

where r is a 3D vector ($[x,y,z]^T$) representing a point in a 3D space or a 2D vector ($[x,y]^T$) in 2D. $n(r)$ is a spatial independent Gaussian distributed noise, and the operator $\otimes$ denotes a convolution. The goal of correction is to restore the true object $o(r)$ by deconvolution of the observed CBCT $i(r)$. It becomes a least square minimization denoted as

$$E^{Deconvolution} = \sum_r (i(r) - o(r) \otimes h(r))^2 \quad (2)$$

Solving $o(r)$ by minimization of E usually leads to noise amplification and severe ring artifacts. In order to find a unique and stable solution for E, prior knowledge about $o(r)$ is required to regularize the minimization.

Viewing x-ray CBCT as a probabilistic mapping of the objects' interaction with x-rays, scatter correction can be considered as maximization of a posteriori probability to obtain the true object o providing the observed image i, point spread function (PSF), and prior information about object o. According to Bayesian' theorem, a posteriori probability can be expressed as

$$p(o \mid i) = p(i \mid o)\, p(o) \,/\, p(i) \quad (3)$$

$p(o \mid i)$ is a posteriori probability of a object o accompanied with an observation i. $p(i)$ is the probability of observing CBCT i and is a constant here. $p(o)$ is the prior information about true objects. $p(i \mid o)$ is the posterior probability density of observing image i given true object o. Based on the assumption of signal-independent Gaussian noise model, $p(i \mid o)$ is denoted as

$$p(i \mid o) = \exp\left(-\frac{1}{2\sigma_n^2} \sum_r (i(r) - o(r) \otimes h(r))^2\right) \quad (4)$$

where σ_n^2 is a Gaussian noise variance which could be estimated from background or uniform tissue regions and assumed to be spatial independent.

2.2 CT-based Patch-wise Prior Information

In a Bayesian framework, prior information regarding the true object is important for artifact correction. We modeled the true object as a MRF and described the prior information as intensity interaction between voxels in order to account for the regularization of local smoothness. The prior information is described by Gibbs formulation as

$$p(o) = \frac{1}{G} \exp\left(-\eta \sum_{c \in C} U_c(o)\right) \quad (5)$$

where $U_c(o)$ is Gibbs potential defined on each possible set c of voxels, G is a normalizing factor, and the cliques C determine the range of voxel interactions. In the proposed method, only the interaction between neighboring voxels is considered and the prior information is expressed as

$$p(o) = \frac{1}{G}\exp(-\eta \sum_{r} \sum_{s \in N(r)} w(r,s)(o(r) - o(s))^2) \quad (6)$$

where $N(r)$ is neighborhood around voxel r, that is, 26 voxels in 3D or 8 pixels in 2D, and $w(r, s)$ is a weighting coefficient. The prior information constrains, the local smoothness between neighboring voxels by the square of intensity difference, and $w(r, s)$ determines the weight to enforce this regularization.

Originated from the non-local strategy which has been widely used in the computer vision area, such as image denoising and super resolution [17, 18], most patch-based methods work in a non-local manner [19]. The similarity between two pixels r and s depends on the similarity of the intensity gray level vectors $o(P_r)$ and $o(P_s)$, where P_k denotes a patch of fixed size and centered at a pixel k. The pixels with a similar grey level patch to $o(P_r)$ have larger weights in the average. In order to reduce the computational time, here we performed a preselection of the patches. By using simple statistics such as mean or variance, it is possible to discard the most dissimilar patches. In the proposed approach, we used luminance and contrast criteria to achieve the patch preselection. Based on the well-known structural similarity measure (SSIM) [20, 21], the preselection procedure can be written as follows:

$$ss = \frac{2\mu_r\mu_s}{\mu_r^2 + \mu_s^2} \times \frac{2\sigma_r\sigma_s}{\sigma_r^2 + \sigma_s^2} \quad (7)$$

where μ represents the means and σ represents the standard deviations of the patches centered on voxel r and voxel s. If the value of ss is greater than a given threshold th, the intensity distance between patches P_r and P_s is computed. The threshold th was set to 0.90 in this study. This value was chosen empirically because it provides a good balance between accuracy and computational time reduction. Patch mean and variance were precomputed as maps of local means and local variances that avoid multiple computations.

Depending on the similarity between the patches surrounding r and s, these weights $w(r, s)$ are computed as [22, 23],

$$w(r,s) = \begin{cases} \frac{1}{Z(r)}\exp(-\frac{\left\|o(P_r) - o(P_s)\right\|_2^2}{l^2}) & if \quad ss > th \\ 0 & else \end{cases} \quad (7)$$

with $Z(r)$ is the normalizing constant

$$Z(r) = \sum_s \exp\left(-\frac{\left\|o(P_r) - o(P_s)\right\|_2^2}{l^2}\right) \quad (8)$$

and the parameter l controls the decay of the exponential function and therefore the decay of the weights as a function of the Euclidean distances. $\|\cdot\|_2$ is the normalized $L2$ norm (i.e., normalized by the number of elements) computed between each intensity of the elements of the patches P_r and P_s. The non-local mean not only compares the grey level in a single point but the geometrical configuration in a whole patch [24]. We used patches with 5×5 pixels here.

2.3 CT-guided Scatter Correction

The true object is restored by maximizing a posteriori probability as

$$o = \underset{o}{\operatorname{argmax}}\, p(o \mid i) = \underset{o}{\operatorname{argmax}}[\, p(i \mid o)\, p(o)] \quad (9)$$

With the definition of $p(i \mid o)$ and $p(o)$, the maximization becomes a minimization of the following cost function:

$$o = \underset{o}{\operatorname{argmin}}\, E(o) = \underset{o}{\operatorname{argmin}}\left[\sum_r (i(r) - o(r) \otimes h(r))^2 + \eta \sum_r \sum_{n \in N(r)} w(r,n)(o(r) - o(n))^2\right] \quad (10)$$

where η is a parameter to balance the convolution and the MRF smoothness constraint, which is chosen heuristically in this study but will be simultaneously estimated based on image noise distribution.

The correction o is sought by minimization of the cost function E using a conjugate gradient (CG) method. CG minimization requires analytical derivatives of the cost function with respect to the true object in each voxel. Because PSF h is a symmetric Gaussian function, the correlation is equivalent to a convolution operation. It is widely accepted that x-ray CBCT PSF can be approximated as an anisotropic 3D Gaussian function that is written as

$$h(r) = \frac{1}{(2\pi)^{3/2}\sigma_x\sigma_y\sigma_z}\exp\left[-\frac{1}{2}\left(\frac{x^2}{\sigma_x^2} + \frac{y^2}{\sigma_y^2} + \frac{z^2}{\sigma_z^2}\right)\right] = \exp\left(-\frac{x^2}{2\sigma_x^2}\right)\exp\left(-\frac{y^2}{2\sigma_y^2}\right)\exp\left(-\frac{z^2}{2\sigma_z^2}\right) \quad (11)$$

where $\sigma = [\sigma_x, \sigma_y, \sigma_z]$is the standard deviation in each direction. The PSF can be measured by fitting the Gaussian function to CBCT images of a point object [25].

3. EXPERIMENTS AND RESULTS

This technique was evaluated using Catphan 404 with multiple inserts. Contrast-to-noise ratios (CNR) and signal-to-noise ratios (SNR) [26] of the different inserts, and the image spatial non-uniformity (ISN) [27] in selected volume of interests (VOIs) were calculated to assess the proposed correction method. The CNR after our correction increased by a factor of 1.96, 3.22, 3.20, 3.46, 3.44, 1.97 and 1.65 for the Air, PMP, LDPE, Polystryrene, Acrylic, Delrin and Teflon inserts. While the SNR increased by a factor 1.05, 2.09, 1.71, 3.95, 2.52, 1.54 and 1.84 for the above inserts, respectively. The ISN decreased from 21.1% to 4.7% in the corrected images. All values of CNR, SNR and ISN in the corrected CBCT image were much closer to those in the planning CT images. Figure 1 shows the corrected results of Catphan phantom, which includes the planning CT, the CBCT image before and after correction, and fused images between CT and original/corrected CBCT. Figure 2 displays a profile through the planning CT, the original CBCT and the corrected CBCT images. The results demonstrated that the proposed method significantly reduces the relevant artifacts and recovers CT numbers.

4. CONCLUSION

We have developed a novel artifact correction method to improve CBCT imaging for quantitative use. In this method we integrated the prior x-ray image information from co-registered planning CT images and the MRF smoothness constraint into a Bayesian deconvolution framework to iteratively perform scatter artifact correction for CBCT mages. We demonstrated that the proposed CT-guided correction method could significantly reduce scatter artifacts and improve the image quality. This method has great potential to correct CBCT images allowing its quantitative use in adaptive radiotherapy.

ACKNOWLEDGEMENTS

This research is supported in part by the Department of Defense (DoD) Prostate Cancer Research Program (PCRP) Award W81XWH-13-1-0269 and Dunwoody Golf Club Prostate Cancer Research Award, a philanthropic award provided by the Winship Cancer Institute of Emory University.

REFERENCES

[1]. Giles W, Bowsher J, Li H et al., “Crescent artifacts in cone-beam CT,” Medical Physics, 38(4), 2116–2121 (2011). [PubMed: 21626944]

[2]. Niu TY, Al-Basheer A, and Zhu L, “Quantitative cone-beam CT imaging in radiation therapy using planning CT as a prior: First patient studies,” Medical Physics, 39(4), 1991–2000 (2012). [PubMed: 22482620]

[3]. Schulze R, Heil U, Gross D et al., “Artefacts in CBCT: a review,” Dentomaxillofacial Radiology, 40(5), 265–273 (2011). [PubMed: 21697151]

[4]. Yang XF, Wu SY, Sechopoulos I et al., “Cupping artifact correction and automated classification for high-resolution dedicated breast CT images Xiaofeng Yang and Shengyong Wu,” Medical Physics, 39(10), 6397–6406 (2012). [PubMed: 23039675]

[5]. Yang X, Sechopoulos I, and Fei B, “Automatic Tissue Classification for High-resolution Breast CT Images Based on Bilateral Filtering,” Proc SPIE Int Soc Opt Eng, 7962, 79623H (2011).

[6]. Li H, Mohan R, and Zhu XR, “Scatter kernel estimation with an edge-spread function method for cone-beam computed tomography imaging,” Physics in Medicine and Biology, 53(23), 6729–6748 (2008). [PubMed: 18997269]

[7]. Rinkel J, Gerfault L, Esteve F et al., “A new method for x-ray scatter correction: first assessment on a cone-beam CT experimental setup,” Physics in Medicine and Biology, 52(15), 4633–4652 (2007). [PubMed: 17634655]

[8]. Neitzel U, “Grids or air gaps for scatter reduction in digital radiography: a model calculation,” Med Phys, 19(2), 475–81 (1992). [PubMed: 1584148]

[9]. Sorenson JA, and Floch J, “Scatter Rejection by Air Gaps - an Empirical-Model,” Medical Physics, 12(3), 308–316 (1985). [PubMed: 4010635]

[10]. Floyd CE, Baydush AH, Lo JY et al., “Scatter Compensation for Digital Chest Radiography Using Maximum-Likelihood Expectation Maximization,” Investigative Radiology, 28(5), 427–433 (1993). [PubMed: 8496036]

[11]. Jarry G, Graham SA, Moseley DJ et al., “Characterization of scattered radiation in kV CBCT images using Monte Carlo simulations,” Medical Physics, 33(11), 4320–4329 (2006). [PubMed: 17153411]

[12]. Ning R, Tang X, and Conover D, “X-ray scatter correction algorithm for cone beam CT imaging,” Med Phys, 31(5), 1195–202 (2004). [PubMed: 15191309]

[13]. Zhu L, Bennett NR, and Fahrig R, “Scatter correction method for X-ray CT using primary modulation: Theory and preliminary results,” Ieee Transactions on Medical Imaging, 25(12), 1573–1587 (2006). [PubMed: 17167993]

[14]. Hansen VN, Swindell W, and Evans PM, “Extraction of primary signal from EPIDs using only forward convolution,” Medical Physics, 24(9), 1477–1484 (1997). [PubMed: 9304576]

[15]. Yang X, Liu T, Dong X et al., “A Planning CT-Guided Scatter Artifact Correction Method for CBCT Images,” Medical Physics, 43(6), 3799–3799 (2016).

[16]. Chen ZK, and Ning RL, “Three-dimensional point spread function measurement of cone-beam computed tomography system by iterative edge-blurring algorithm,” Physics in Medicine and Biology, 49(10), 1865–1880 (2004). [PubMed: 15214529]

[17]. Coupe P, Yger P, Prima S et al., “An optimized blockwise nonlocal means denoising filter for 3-D magnetic resonance images,” Ieee Transactions on Medical Imaging, 27(4), 425–441 (2008). [PubMed: 18390341]

[18]. Yang XF, Jani AB, Rossi PJ et al., “Patch-Based Label Fusion for Automatic Multi-Atlas-Based Prostate Segmentation in MR Images,” Medical Imaging 2016: Image-Guided Procedures, Robotic Interventions, and Modeling, 9786, (2016).

[19]. Coupe P, Manjon JV, Fonov V et al., “Patch-based segmentation using expert priors: Application to hippocampus and ventricle segmentation,” Neuroimage, 54(2), 940–954 (2011). [PubMed: 20851199]

[20]. Wang Z, Bovik AC, Sheikh HR et al., “Image quality assessment: From error visibility to structural similarity,” Ieee Transactions on Image Processing, 13(4), 600–612 (2004). [PubMed: 15376593]

[21]. Yang XF, Wu N, Cheng GH et al., “Automated Segmentation of the Parotid Gland Based on Atlas Registration and Machine Learning: A Longitudinal MRI Study in Head-and-Neck Radiation Therapy,” International Journal of Radiation Oncology Biology Physics, 90(5), 1225–1233 (2014).

[22]. Buades A, Coll B, and Morel JM, “A non-local algorithm for image denoising,” 2005 IEEE Computer Society Conference on Computer Vision and Pattern Recognition, Vol 2, Proceedings, 60–65 (2005).

[23]. Yang XF, Jani AB, Rossi PJ et al., “A MRI-CT Prostate Registration Using Sparse Representation Technique,” Medical Imaging 2016: Image-Guided Procedures, Robotic Interventions, and Modeling, 9786, (2016).

[24]. Yang XF, Rossi PJ, Jani AB et al., “3D Transrectal Ultrasound (TRUS) Prostate Segmentation Based on Optimal Feature Learning Framework,” Medical Imaging 2016: Image Processing, 9784, (2016).

[25]. Garayoa J, and Castro P, “A study on image quality provided by a kilovoltage cone-beam computed tomography,” Journal of Applied Clinical Medical Physics, 14(1), 239–257 (2013).

[26]. Yang X, Torres M, Kirkpatrick S et al., “Ultrasound 2D strain estimator based on image registration for ultrasound elastography,” Proc. SPIE, Medical Imaging 2014: Ultrasonic Imaging and Tomography, 9040, 904018–904018-10 (2014).

[27]. Yang X, and Fei B, “A wavelet multiscale denoising algorithm for magnetic resonance (MR) images,” Meas Sci Technol, 22(2), 25803 (2011). [PubMed: 23853425]

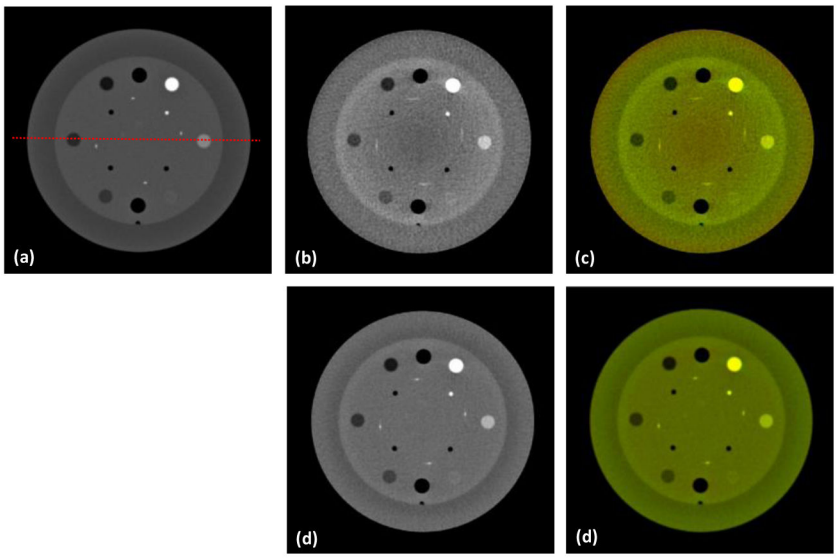

Figure 1.

Results of the Catphan phantom. (a) CT image, (b) CBCT image, (c) fused image between CT (red) and original CBCT images (green), (d) corrected CBCT image, and (e) fused image between CT (red) and corrected CBCT images (green).

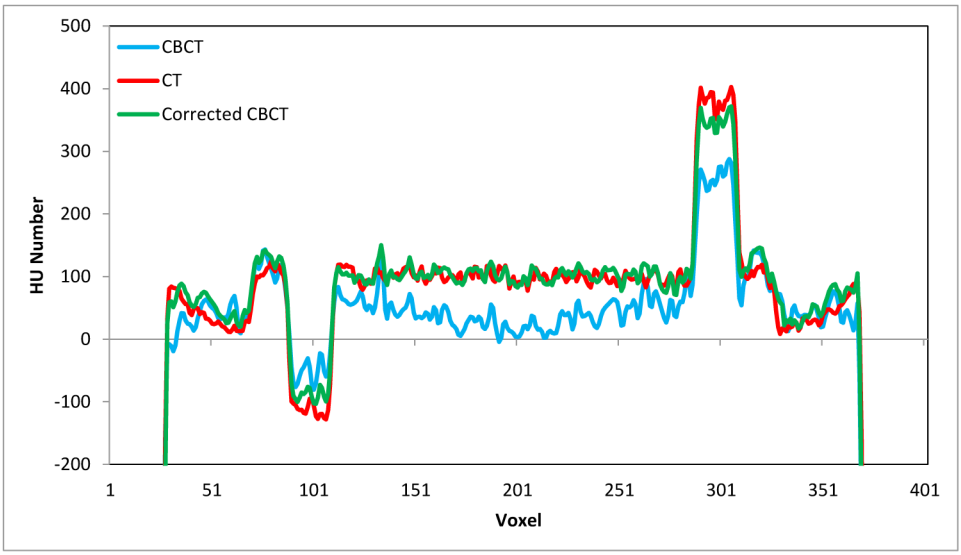

Figure 2.
The profile comparison of CT, CBCT and corrected CBCT image through the red dotted line in Figure 1.